Ocean Systems Engineering, *Vol. 15, No. 2 (2025) 173-194*
https://doi.org/10.12989/ose.2025.15.2.173

Data-driven design and optimization of multi-chamber oscillating water column using CFD and machine learning

S. Prasanna[1], Yoon Hyeok Bae[2] and Poguluri Sunny Kumar[*1]

[1]*Department of Ocean Engineering, Indian Institute of Technology Madras, Chennai 600036, India*
[2]*Department of Mechanical and System Design Engineering, Hongik University, Seoul 04066, Republic of Korea*

(Received March 17, 2025, Revised June 2, 2025, Accepted June 19, 2025)

Abstract. This study presents a comprehensive data-driven approach for the design and optimization of multi-chamber oscillating water column (OWC) wave energy converters by integrating high-fidelity computational fluid dynamics (CFD) simulations with machine learning (ML) techniques. The CFD model was rigorously validated against experimental data from literature results, with good agreement observed in both hydrodynamic efficiency and power output. Further, a large input data has been generated with distinct simulation cases, spanning single-, double-, and triple-chamber chamber configurations under various wave conditions with *kh* ranging from 2.0 s to 5.5 s, were conducted. The CFD-generated dataset was employed to train several ML models—polynomial regression, decision trees, random forest, XGBoost, support vector regression, and multilayer perceptron. XGBoost demonstrated better performance compared to the other machine learning models evaluated. Furthermore, to identify the optimal design configuration, Latin Hypercube Sampling was employed to randomly generate 1,000 distinct OWC configurations, which were then evaluated using the XGBoost model. The top ten configurations were identified, with the highest predicted power output of 36.40 W obtained from the dual-chamber OWC configuration. These findings confirm the potential of ML-driven models to significantly reduce computational cost and accelerate the design of efficient wave energy systems.

Keywords: CFD; design optimization; ML models; multi-chamber OWC; XGBoost

1. Introduction

As global demand for clean, sustainable energy grows, wave energy has attracted increasing attention as a promising solution. Ocean waves are a crucial yet underutilized source of renewable energy, with the potential to provide a stable and substantial supply of electrical power, particularly in regions with long, exposed coastlines (Karimirad 2014, Singh *et al.* 2022, Kassayeva *et al.* 2024). Unlike solar or wind energy, which depend on intermittent weather conditions, ocean waves offer a more consistent source of power (Karimirad 2014). Although ocean waves hold immense potential as an offshore renewable energy source, the technology required to harness their power on a commercial scale remains in its early stages. Over the past few decades, researchers have made significant strides in exploring wave energy, experimenting

*Corresponding author, Assistant Professor, E-mail: pskumar@iitm.ac.in

http://www.techno-press.org/?journal=ose&subpage=7 ISSN: 2093-6702 (Print), 2093-677X (Online)

with various technologies and designs aimed at capturing the ocean's power (Faedo and Ringwood 2024, and Yang *et al.* 2024).

In general, wave energy extraction relies on a moving device, which can be either floating, submerged, or fixed. One common method is the oscillating water column (OWC), where the rise and fall of water levels inside a chamber create pressure differences between the trapped air and the external atmosphere. This pressure fluctuation drives air through a turbine, converting wave motion into mechanical energy, which is then transformed into electricity. OWC is a well established concept since 1947 and many have tested on prototype scale and some or near the commericalization (Heath 2012, Falcão and Henriques 2016, Zhao and Ning 2024, Gayathri *et al.* 2024).

Recent research has significantly addressed the influence of various physical parameters on the performance of OWC devices, using a combination of experimental, numerical, and analytical approaches. Studies by Malara and Arena (2013), Mahnamfar and Altunkaynak (2017), Ning *et al.* (2014), Moñino *et al*. (2017), Kim *et al.* (2022), Rosati *et al.* (2022), Liu *et al*. (2022), Zabihi *et al.* (2019), and Han *et al*. (2021) have provided substantial insights into the factors affecting OWC efficiency and optimization, and highlight some of the current challenges and opportunities in the field. Mahnamfar and Altunkaynak (2017), who investigated the optimization of OWC systems to maximize power extraction. Using Flow 3D, a computational fluid dynamics (CFD) software, they modeled the behavior of the OWC under four different regular wave conditions and varying water depths. Their experimental are validated with the numerical simulations. The performance evaluation of both the experimental and numerical results was carried out using the Nash-Sutcliffe coefficient of efficiency, which is a common statistical measure used to assess the predictive accuracy of hydrodynamic models. The results from both the experiments and the simulations showed good agreement, confirming the reliability of the Flow 3D model in predicting OWC performance under different conditions. Sing *et al.* (2020) further explored the dynamics of floating OWCs integrated with a tension leg mooring system. Their laboratory experiments, conducted under both regular and irregular wave conditions, revealed that the hydrodynamic efficiency of the system was particularly sensitive to the model's motion at wave frequencies below 4.15 rad/s. It is also reported that the performance of the system was hampered by excessive motion, which reduced the efficiency of the power extraction process. The study also emphasized that CFD simulations provided more accurate predictions of hydrodynamic performance compared to linearized models such as potential flow theories. However, the computational cost of running detailed CFD simulations remains a limitation, especially when applied to large datasets or multiple configurations, which hinders their widespread application in the design optimization of OWC (Cui *et al.* 2019, Shalby *et al.* 2019, Filianoti *et al.* 2018, Gurnari *et al.* 2022).

The need for more efficient optimization methods has led to the integration of artificial intelligence (AI) techniques, particularly neural networks (NN), into the optimization process for OWCs (George *et al.* 2012, Vipin *et al.* 2023, Natarajan *et al.* 2024, Rao *et al.* 2024). Neural networks can effectively model complex, nonlinear relationships between design parameters and performance metrics. Their advantage lies in their ability to process large amounts of data once they are properly trained and validated with existing experimental or numerical results. This is particularly beneficial for optimizing OWCs across a wide range of operating conditions, as they can generalize from a relatively small set of training data and provide solutions for a vast number of design scenarios (George *et al.* 2012, Natarajan *et al.* 2024). However, as pointed out by several researchers, the use of NN to optimize OWC systems remains relatively underdeveloped, with many studies being limited to a linear model are used for the generation of data and commented on

the performance (Natarajan *et al.* 2024, Rao *et al.* 2024). Rao *et al*. (2024) conducted a comprehensive comparison of AI techniques, specifically focusing on random forest and NN models, for the optimization of power generation in OWC devices. The study considered several key design parameters for optimization, including front wall depth, chamber length, and wave period. These parameters were evaluated using a linear boundary element method (BEM), which is commonly employed in wave energy modeling to solve for the interactions between the fluid and structure. The results indicated that the NN model outperformed the random forest model in terms of accuracy and predictive capability for power generation optimization in OWCs. Similarly, Natarajan *et al*. (2024) explored the application of NN models to a more complex OWC system, specifically one integrated with an inclined barrier in front, operating under irregular wave conditions. The data preparation for this study was based on linear potential flow theory and utilized a dual BEM to model the hydrodynamics of the system. The study found that the NN model was highly effective in learning and predicting the complex nonlinear behavior of the OWC system. With high accuracy, the NN model was able to predict the optimal design parameters and identify the best installation locations for the OWC device, offering valuable insights into the feasibility of different configurations.

The computational burden of performing detailed CFD simulations for every design iteration is significant, especially when considering the large number of design parameters that need to be explored. This limitation has motivated researchers to combine CFD simulations with machine learning (ML) model based optimization approaches. By doing so, the ML model can act as a surrogate model to predict system behavior based on a limited number of simulations, drastically reducing the computational time required for optimization while still maintaining a high level of accuracy. The preliminary motivation behind the current work is to build upon this idea by incorporating ML models into the OWC optimization process. The goal is to explore how well-trained ML models can be used to approximate the results of expensive CFD simulations, making it feasible to optimize the performance of OWCs across a larger parameter space without incurring prohibitive computational costs. Once a ML model is trained on experimental or numerical data, it can be applied to quickly explore a wide range of design variations, allowing for more efficient and effective optimization of OWC systems in real conditions.

2. Problem description

2.1 Physical configuration

The OWC device considered in this research is based on a scaled model with a scale ratio of 1:12.5, following the experimental setup of Morris-Thomas *et al.* (2007). The device consists of chamber designed to capture wave energy through the oscillation of water columns. The dimensions are selected to prevent energy transfer beyond the OWC. The chamber width *(w)* of a single OWC is 0.64 m, and as the number of chambers increases, each chamber's width is equal to the total width divided by the number of chambers. The effect of the PTO device is modeled by a circular vent (orifice) at the upper right end. Key parameters include a front wall submergence (d), which is also equivalent to and sometimes when referring to the chamber_1 depth (d_1), and has a value of 0.15 m, and diameter (ϕ) of 5 mm, and a chamber width (w) of 0.64 m. Each subscript in the notations corresponds to the chamber number. Fig. 1 illustrates the schematic configuration of the OWC device used in this study. The chamber width is divided into two equal halves,

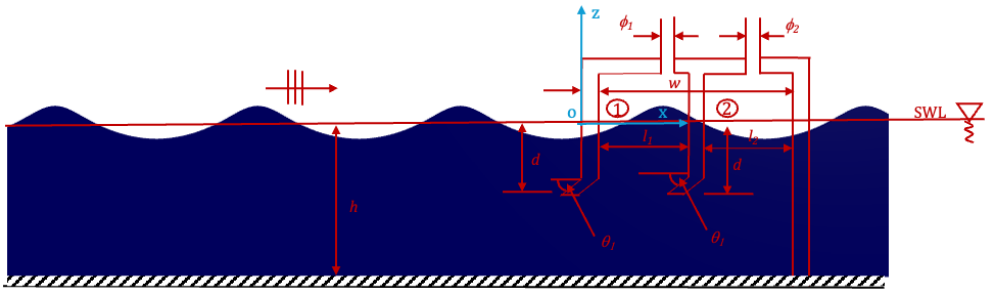

Fig. 1 Schematic representation of a multi-chamber OWC in regular wave conditions

Table 1 Single-chamber OWC simulation cases

Front wall Depth	Orientation (θ)	No. of wave periods (T_1-T_{10})	Total Cases
d_1	0°	10	10
d_1	30°	10	10
d_2	0°	10	10
d_3	30°	10	10
	Total		**40 Cases**

each measuring l_1 (= l_2). The figure also illustrates the lip-wall oriented at an angle θ_1 of 15º and it should be noted that the thickness of the lip-wall is kept constant throughout all simulations. The water depth (h) of 0.92 m is maintained.

2.2 Simulation cases

The performance of the OWC device is significantly influenced by factors such as the front wall depth, number of chambers, sidewall orientation, and orifice diameter, all of which affect the amount of wave energy captured. To thoroughly assess the device's performance under various conditions, extensive CFD simulations were performed by altering key parameters. Table 1 provides a summary of the simulation cases for the single-chamber OWC configuration, with variations in sidewall depth and orientation. Similarly, Tables 2 and 3 present the simulation cases for the dual-chamber and triple-chamber configurations, respectively. The OWC is exposed to a range of wave periods, specifically: T_1 is 2.0 s, T_2 is 2.5 s, T_3 is 3.0 s, T_4 is 3.25 s, T_5 is 3.5 s, T_6 is 3.75 s, T_7 is 4.0 s, T_8 is 4.5 s, T_9 is 5.0 s, and T_{10} is 5.5 s. Where $d_2 = 2\times d_1$ and $d_3=3\times d_1$. In the present study, the selection of wave periods is based on design wave conditions relevant to Indian coastal waters, with a particular focus on a potential deployment site along the coast of Kerala (Ananthu *et al.* 2025, Chowdhury *et al.* 2019). To ensure the relevance and applicability of the study, the chosen model scale is designed to cover a broad range of these design wave conditions. For consistency in the model simulations, a constant wave height of 0.12 m is used across all cases.

Table 2 Dual-chamber OWC simulation cases

Front wall depth 1	Front wall depth 2	Orientation (θ)	No. of wave periods (T_1-T_{10})	Orifice Diameter (ϕ)	Total Cases
d_1	d_1	0°	9	5mm	9
d_2	d_2	0°	9	5mm	9
d_3	d_3	0°	9	5mm	9
d_2	d_1	0°	10	5mm	10
d_1	d_2	0°	6	5mm	6
d_1	d_2	30°	9	1mm	9
d_1	d_2	30°	7	3mm	7
d_1	d_2	30°	10	5mm	10
d_1	d_2	30°	7	7mm	7
d_1	d_2	30°	10	9mm	10
		Total			**86 Cases**

Table 3 Triple-chamber OWC simulation cases

Sidewall 1 Depth	Sidewall 2 Depth	Sidewall 3 Depth	Orientation (θ)	No. of wave periods (T_1-T_{10})	Total Cases
d_1	d_1	d_1	0°	10	10
d_2	d_2	d_2	0°	10	10
d_3	d_3	d_3	0°	10	10
d_1	d_2	d_3	0°	10	10
d_3	d_2	d_1	0°	10	10
		Total			**50 Cases**

In total, 176 distinct simulation cases were analyzed across the three configuration studies. For each case, covering a range of wave period from 2.0 s to 5.5 s. This comprehensive approach allows for a thorough investigation of the influence of geometric parameters, orientation, and orifice diameter characteristics on the performance of multi-chamber OWC devices under various regular wave conditions. Some wave periods were omitted from the final simulations see Tables 1-3, as they fall within the small wave period range, where chamber pressure fluctuations and wave energy concentrations were low. These low-power conditions were excluded to focus on practically significant, high-power scenarios. Importantly, wave periods contributing dominant power were carefully considered and are well represented to ensure the study's relevance to practical applications.

2.3 Power extraction

The pneumatic power available at the orifice (P_{out}) per wave cycle of period T is calculated as the time-averaged product of the measured pressure inside the chamber P_{ch}, the velocity of the oscillating air column (v_{ch}), and the chamber's cross-sectional area (A), as given by

$$P_{out} = \langle P_{ch} \cdot v_{ch} \cdot A \rangle \tag{1}$$

where the time average $\langle\cdot\rangle$ is taken over complete wave cycle of period T. For the OWC device, the air inside the chamber is assumed to behave as incompressible, as the scale of the device is small enough for compressibility effects to be negligible (see Elhanafi and Kim 2018, López *et al*. 2020, Zhao and Ning 2024). The incident wave energy flux is calculated as

$$P_{in} = \frac{1}{4}\rho g \frac{H^2}{2} \frac{\omega}{k}\left(1 + \frac{2kh}{sinh2kh}\right) \tag{2}$$

where, ρ represents the liquid density, which is assumed to be of fresh water, and g being the acceleration due to gravity, H is the wave amplitude, ω is the angular frequency of the incident, k is the wavenumber of the incident wave and final hydrodynamic efficiency is given by

$$\eta_{owc} = \frac{P_{out}}{P_{in} w} \tag{3}$$

where w is the characteristic width of the OWC device. These formulations are used to assess the performance of various multi-chamber OWC configurations and determining optimal design parameters through CFD simulations, followed by ML analysis.

3. Numerical model

Machine learning methods provide a significant advantage in their ability to detect and understand complex, nonlinear relationships hidden within input data. The nature and origin of the input data used in machine learning models are of paramount importance, as they directly influence the quality and accuracy of the results. In past research, however, the input data typically relied on models based on linear or weakly nonlinear assumptions, and some used fully nonlinear models or experimental data. The former models were often simpler and less computationally demanding, but they could not fully account for the intricate nonlinearities present in systems. On the other hand, the latter approaches, while more accurate, are time-consuming and complex in generating large datasets. In the present study, takes an approach by using fully nonlinear simulations to generate the input data. Specifically using CFD simulations are employed using Star-ccm+, which involve solving the incompressible Navier-Stokes equations, a set of fundamental equations governing fluid flow, along with the continuity equation are given in Eqs. (4) and (5). The use of the finite volume method (FVM) for solving these equations allows for a more accurate representation of fluid flow over irregular waves and under varying wave conditions.

$$\frac{\partial \mathbf{u}}{\partial t} + (\mathbf{u},\nabla)\mathbf{u} = -\frac{\nabla \rho}{\rho} + g + v\nabla^2\mathbf{u} \tag{4}$$

$$\nabla, \mathbf{u} = 0 \tag{5}$$

where ρ represents the liquid density, which is assumed to be that of fresh water, and g being the acceleration due to gravity. The nonlinear governing equations outlined above are solved iteratively in a sequence, for the fluid velocity vector $\mathbf{u}$, and then for the pressure p, using a segregated flow solver approach. The pressure-velocity coupling is resolved using the SIMPLE (Semi-Implicit Method for Pressure-Linked Equations) algorithm. For this study, both laminar and turbulent flow models were numerically tested to evaluate their effects on the results. However, the variations between the two models were found to be negligible for the current problem.

Consequently, the study is based exclusively on the laminar flow model, as it provides a sufficiently accurate representation of the system's behavior within the scope of this analysis.

The present problem is formulated through a two-phase flow analysis, employing a volume-of-fluid (VOF) formulation to capture the behavior and interaction of the phases. In this approach, the phase volume fraction properties are used to differentiate the various media present, which in this case are identified as water, air, and a mixed phase. The VOF method tracks the interface between the two phases by solving a transport equation for the volume fraction of each phase across the computational domain. The volume fraction of water is denoted by α_w, and it represents the proportion of the water phase at any given location in the domain. This volume fraction is governed by the following scalar transport equation

$$\frac{\partial \boldsymbol{\alpha_w}}{\partial t} + (\mathbf{u},\nabla)\alpha_w = 0 \tag{6}$$

This equation tracks the evolution of the water phase within the domain, accounting for both the advection due to the velocity field and the diffusion of the water phase across the interface. The solution of this equation provides the distribution of water and air phases at each point in the flow domain, which is essential for accurately simulating the interaction between the phases and the resulting flow dynamics.

3.1 Computational domain setup

The computational domain was designed to replicate upstream conditions, with a horizontal length of 5 times the wavelength (5×λ) and a vertical height of 2.5 m, all for a fixed water depth of 0.92 m. The present simulations are conducted in a two-dimensional framework, where a unit depth is assumed in the *y*-direction. This approach neglects any three-dimensional effects, focusing solely on variations in the *x*–*z* plane. The boundary conditions were specified as follows: a velocity inlet at the left end of the domain, a pressure outlet at the top boundary, and a no-slip condition at the bottom. Additionally, symmetry conditions were applied to both the front and rear sides of the domain. Along with the above boundary conditions, a wave forcing zone was implemented at the inlet to avoid any reflections from the OWC. In this region, the theoretical formulations are forced, while the CFD Reynolds-Averaged Navier–Stokes (RANS) equations are solved for the rest of the domain. A cosine function is used to handle the interface of these two regions, varying from zero to one as it transitions from the theoretical formulations to the CFD region. The right end of the flume is considered a wall.

The generated volume mesh is based on a base cell size of 0.5 m, with target and minimum surface sizes set to 25% and 2% of the base size, respectively. The volume and surface growth rates are set to slow. An automatic mesh was generated using the surface remesher and trimmed cell mesher. A refined mesh has been created near the free surface using anisotropic cells, with the *x* and *z* dimensions set to 1% of the base size. Additionally, an adaptive mesh refinement has been activated to further refine the free surface, adding two more cells both above and below the free surface region, as shown in Fig. 2. An isotropic mesh is used around the OWC, with the mesh divided by 0.5% in and around the OWC. A fine prism-layer mesh, with a total thickness of 0.25% of the base size, is used, divided into four layers to adequately capture the boundary layer at the OWC, ensuring a $y+$ value of less than 3. Though the computational domain size and settings are different from the original experimental setup, they will ensure the simulation accurately represents the system's hydrodynamic behavior numerically.

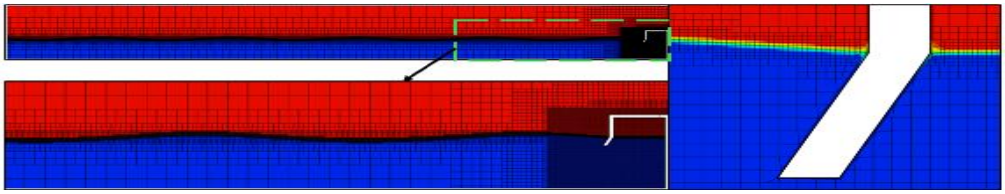

Fig. 2 Mesh generation around the OWC with lip-wall orientation configuration

4. Machine learning

This study utilizes machine learning techniques to optimize the design of the OWC, incorporating some of the most widely used methods in design optimization. Specifically, Polynomial Regression, Decision Trees, Random Forest, Support Vector Regression (SVR), XGBoost (Extreme Gradient Boosting), and Multilayer Perceptron (MLP) regression, each of which offers different levels of interpretability, complexity, and predictive capability. These methods are well-suited for analysing the input data generated by CFD, as described in the previous sections, and are used to train the models for this study.

4.1 Polynomial regression

For relatively simple CFD problems, such as fluid flow in basic geometries, polynomial regression provides an effective starting point. This technique models the relationship between independent variables (x) and a dependent variable (y) as a polynomial of degree n, represented by the equation

$$y = \beta_0 + \beta_1 x + \beta_2 x^2 + \ldots + \beta_n x^n + \varepsilon \tag{7}$$

where $\beta_0, \beta_1, \ldots, \beta_n$, are the regression coefficients, x denotes the independent variables (such as flow parameters), and ε is the error term. The model's coefficients are determined by minimizing the residual sum of squares

$$\min_{\beta} \sum_{i=1}^{m} \left(y_i - \hat{y}_i \right)^2 \tag{8}$$

While the degree of the polynomial limits the model's complexity, polynomial regression offers an interpretable and efficient method for capturing nonlinear relationships without overfitting, provided the polynomial degree is chosen appropriately.

4.2 Decision trees

Decision trees offer a more advanced method by using a non-parametric, supervised learning approach to create a tree-like structure. This structure recursively splits the data based on feature values, with each internal node representing a decision rule. For binary classification, the splitting criterion often uses Gini impurity ($Gini = 1 - \sum p_i^2$), or for regression, Mean Squared Error ($MSE = 1/N \sum (y_i - \hat{y}_i)^2$). Decision trees are known for their high interpretability and can handle both continuous and categorical data. This makes them particularly useful for identifying key features that influence fluid flow behaviour in simpler CFD models.

4.3 Random forest

Random Forest builds on decision trees by employing an ensemble learning technique. It creates multiple decision trees and combines their predictions to improve accuracy. Each tree is trained on a random subset of the data and features, which helps reduce overfitting and increases generalization. For regression tasks, the final prediction is the average of the individual tree predictions is given by Eq. (9). Random Forest's robustness and ability to model complex, high-dimensional relationships make it especially suited for handling large, noisy CFD datasets with numerous interacting parameters.

$$\hat{y} = \frac{1}{T}\sum_{t=1}^{T} \hat{y}_t \tag{9}$$

4.4 Support vector regression

Support Vector Regression is a machine learning technique that aims to find a hyperplane-a multidimensional surface-that best fits the data while maintaining a specified margin of tolerance, denoted by ε (epsilon). Unlike traditional regression models, SVR allows for a margin of error around the hyperplane, within which predictions are considered acceptable and some data points may lie outside this ε-tolerance margin. These are known as slack variables, and they represent how much certain observations deviate from the ideal prediction boundary. To improve model performance, optimization techniques are used to penalize these deviations, reducing their influence on the overall fit. The goal of this optimization is to maximize the margin around the hyperplane while minimizing a loss function, typically a monotonically decreasing function of the model weights. This balance is controlled by a regularization parameter, *C*, which determines the trade-off between achieving a wide margin and minimizing prediction errors from outliers.

4.5 XGBoost

XGBoost is an advanced ensemble method that builds decision trees sequentially, with each new tree focusing on correcting the errors made by previous ones. It optimizes an objective function that combines both loss and regularization terms

$$L(\Theta) = \sum_{i=1}^{n} l(y_i, \hat{y}_t) + \sum_{k=1}^{K} \Omega(f_i) \tag{10}$$

where l is the loss function and $\Omega(f_k)$ controls the complexity of the trees. XGBoost's built-in regularization, efficiency with large datasets, and high predictive accuracy make it especially effective for complex CFD applications, particularly those involving noisy data.

4.6 Multilayer perceptron (MLP) regression

MLP regression emerges as one of the most successful in deep learning models using NN. These networks compute the output of each layer through weighted sums and activation functions

$$a^{(l)} = f\left(W^{(l)}a^{(l-1)} + b^{(l)}\right) \tag{11}$$

where $a^{(l)}$ is the output of layer l, $W^{(l)}$, are the weight matrices, $b^{(l)}$ represents bias terms, and f is the activation function. Neural networks are particularly effective at learning complex patterns and are commonly used in tasks like image recognition, speech processing, and natural language understanding. Although they require significant computational resources and large datasets, NN are ideal for CFD applications involving complex geometries or turbulent flow, as they excel at capturing intricate patterns across multiple abstraction levels.

5. Methodology

The present methodology integrates traditional CFD simulation with machine learning approaches through a systematic workflow consisting of five main phases: pre-processing, CFD simulation, data processing, machine learning, and design optimization (see Fig. 3). This integrated methodology leverages the strengths of both CFD and machine learning approaches. While CFD provides high-fidelity simulation data, machine learning models offer rapid prediction capabilities, enabling efficient design space exploration and optimization. The systematic validation steps throughout the process ensure the reliability of the final results.

The pre-processing phase establishes the foundation for accurate CFD simulation. It begins with the initial CFD model setup, followed by detailed geometry definition and meshing procedures. This phase concludes with the specification of boundary conditions and selection of appropriate physics models. These steps are crucial as they determine the quality and reliability of the subsequent simulation results. During the CFD simulation phase, we conduct analyses across multiple operating conditions to generate a comprehensive dataset. The process includes rigorous solution monitoring and convergence checking to ensure simulation accuracy. Data collection focuses on two primary aspects: pressure distribution and velocity field measurements. These fundamental fluid dynamic parameters are then used to calculate power characteristics, providing a complete picture of the flow behavior by using Eq. (1). The data processing phase bridges the gap between raw CFD results and machine learning model inputs. Feature engineering transforms raw simulation data into meaningful predictors, while feature selection and validation ensure that only the most relevant parameters are retained for model training. This phase is critical for developing efficient and accurate machine learning models. Feature engineering in this study involved calculating the instantaneous power at the chamber center by combining pressure and volumetric flow rate, with the latter derived from the product of flow area and velocity. The flow area was determined using the specific chamber width and depth for each case. For every CFD simulation, this process yielded a time series of instantaneous power values, from which the mean power was extracted and used as the target output in the machine learning model. The input features selected for training the model include chamber depth (d), non-dimensional wave number (kh), orientation angle (θ), and orifice diameter (ϕ). Together, these parameters capture the geometric and flow characteristics influencing power generation. The model was trained to predict the mean power output, serving as a representative measure of performance across simulations. The machine learning phase encompasses three key steps:

Model architecture selection:

- Polynomial regression serves as a baseline model to evaluate initial performance levels.
- Decision trees and random forests are utilized for their transparency, offering clear insights into how features relate to predictions.

- SVR is selected for its strong prediction capability, maintaining low error margins and effectively managing outliers.
- XGBoost is incorporated due to its exceptional performance in regression tasks, utilizing advanced boosting techniques to enhance accuracy and speed.
- MLP regression NN are employed to detect intricate patterns and relationships within the data that might not be captured by simpler models.

Hyperparameter Optimization: We employ K-Fold Cross Validation to tune model parameters, ensuring robust performance across different data subsets.

Model Training and Validation: Models are trained on the processed data and validated against held-out test sets to assess generalization capability.

The final phase focuses on practical application through design optimization. The trained models are used to rapidly explore the design space and make predictions about flow behaviour under various conditions. Multiple performance criteria are simultaneously optimized to identify optimal design configurations. The most promising designs are validated using traditional CFD simulations to ensure reliability of the machine learning predictions.

6. Results and discussion

6.1 Validation

The initial validation was conducted using a single-chamber, as described in the problem section, following the experimental methodology of Morris-Thomas *et al*. (2007). To ensure that

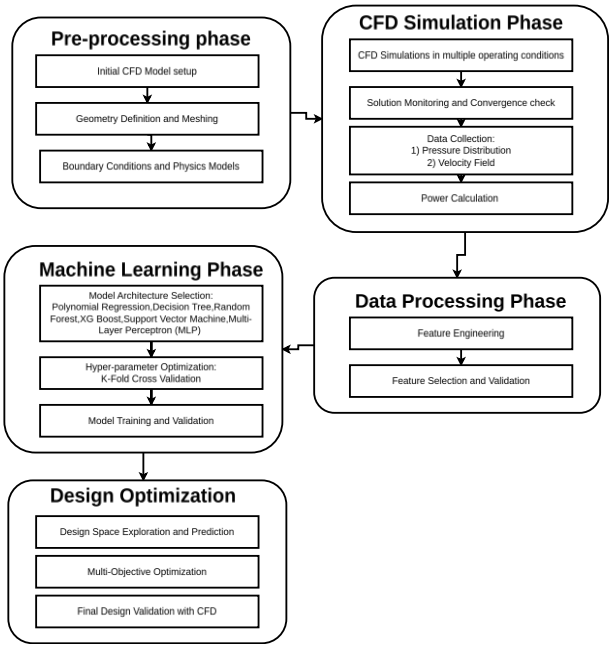

Fig. 3 Present study methodology

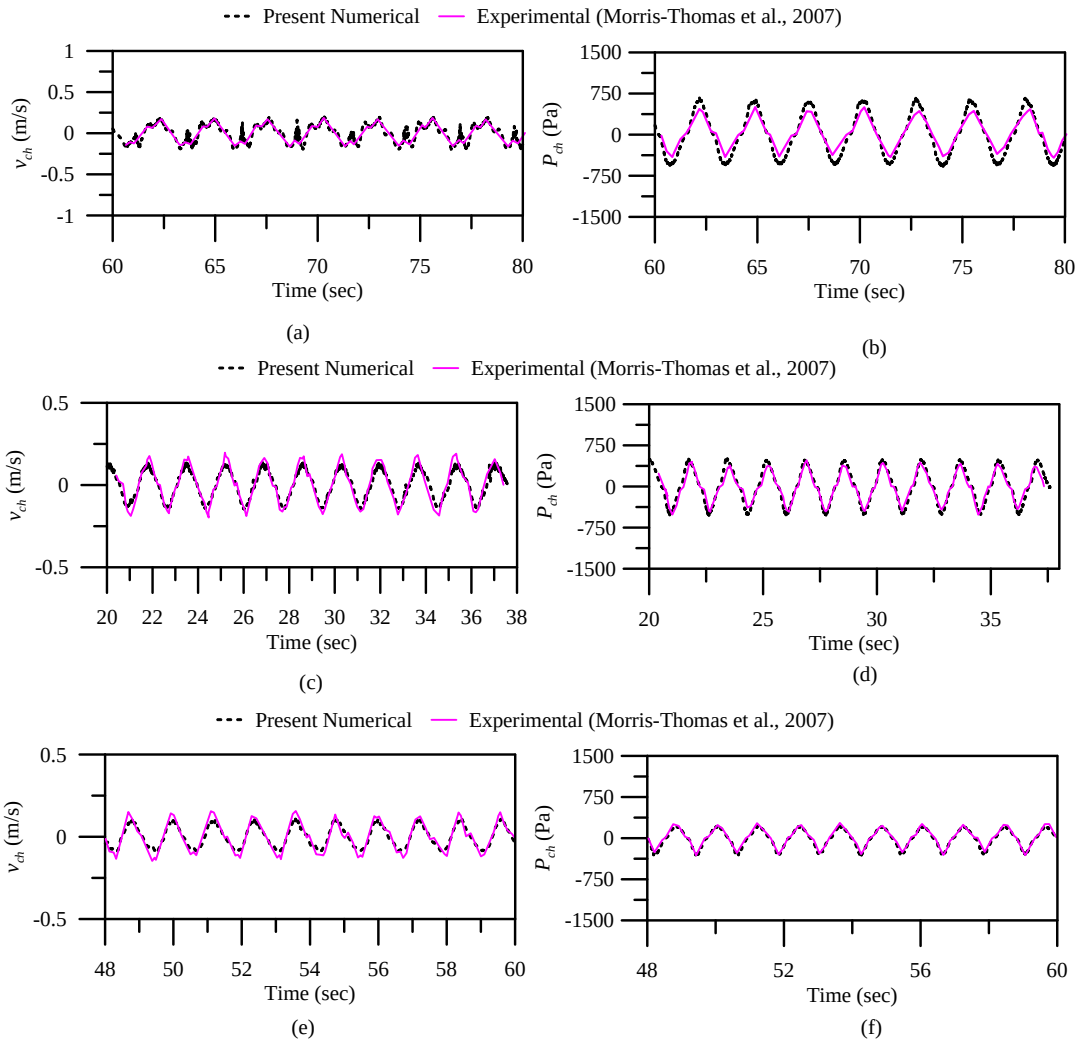

Fig. 4 Validation of velocity and pressure variations within the chamber using the present numerical results compared to the experimental data of Morris-Thomas *et al.* (2007) for (a)&(b) kh =0.52; (c)&(d) kh =1.26 and (e)&(f) with kh =2.50

the system accurately replicate the experimental conditions, the PTO damping mechanism was rigorously calibrated. The orifice size was carefully set to 5 mm to replicate the pressure losses observed in the original experiments, thereby ensuring that the simulated performance of the OWC device closely matched the experimental results. The device spans the entire width of the numerical tank, and the wave conditions on the opposite side of the numerical tank were determined not to have any impact on the simulations. A thorough mesh independence study was conducted, and the final mesh size was determined, as detailed in Section 3.1. This resulted in a base mesh size of 0.548 million. By implementing adaptive meshing, the resolution was refined further by dividing each cell at the free surface by a factor of 2. This refinement strategy ensures

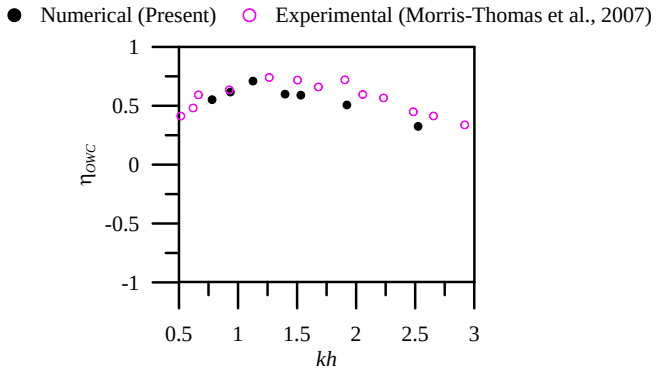

Fig. 5 Variation of efficiency with the range of *kh*

that the *y*+ value remains well below 3, which is essential for accurate near-wall resolution. Initial testing was carried out using three non-dimensional wavelength values (*kh*) of 0.25, 1.26, and 2.5. A wave height of 0.12 m has been selected. These values allowed for a thorough comparison between the simulated results and experimental data under varying wave conditions, facilitating the validation of the numerical model. The comparison of these results with the experimental data is shown in Fig. 4. Among the tested conditions, the *kh* value of 1.26 corresponds to the resonant frequency of the OWC chamber, as identified by Morris-Thomas *et al*. (2007). Excellent agreement between the present numerical results and the experimental findings can be observed, as demonstrated in Fig. 4. Further continuation to the validation, now the variation of hydrodynamic efficiency has been compared with the experimental results for the range of *kh* values as shown in Fig. 5. Based on the Eq. (3) the estimated efficiency for the range of tested values was found to be agrees well in most of the *kh* values. Where the increments of the efficiency was seen up to the *kh* of 1.26 and then on decreases.

6.2 OWC parameter effects

Initially, the test was conducted by varying the number of chambers from single to double to triple while maintaining the chamber total length equal to that of the single-chamber. The power output was calculated and plotted in Figs. 6 and 7, by comparing the single-chamber to both the double- and triple-chambers under a fixed value of *kh* = 1.26, which represents the resonance condition for the single-chamber. The time history plot reveals an unstable pattern, characterized by slight variations in the peaks over time for all configurations, which is clearly illustrated in the zoom-in view plot. When comparing the single-chamber to the double-chamber, the results show a notable increase in power from 24.92 W to 27.37 W, demonstrating a percentage increase of 12% (see Fig. 6). Conversely, the power increase from the double-chamber to the triple-chamber was slightly less, at about 11% (see Fig. 7). This indicates that while there is a significant improvement when moving from single- to double-chamber, the gains become less pronounced as the number of chambers increases further. For the OWC model dimensions considered, increasing the number of chambers to double appears to yield a more substantial increase in power output, suggesting that optimizing the chamber configuration can lead to enhanced effectiveness in power generation.

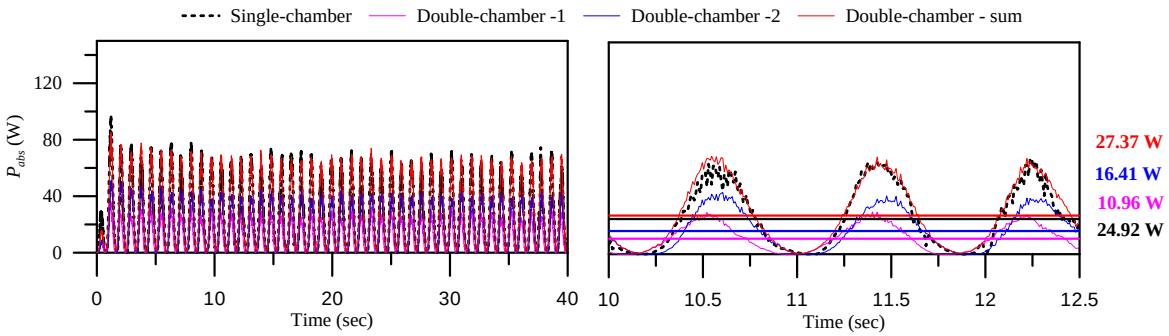

Fig. 6 Power output comparison between single- and double-chamber OWC configurations for kh=1.26

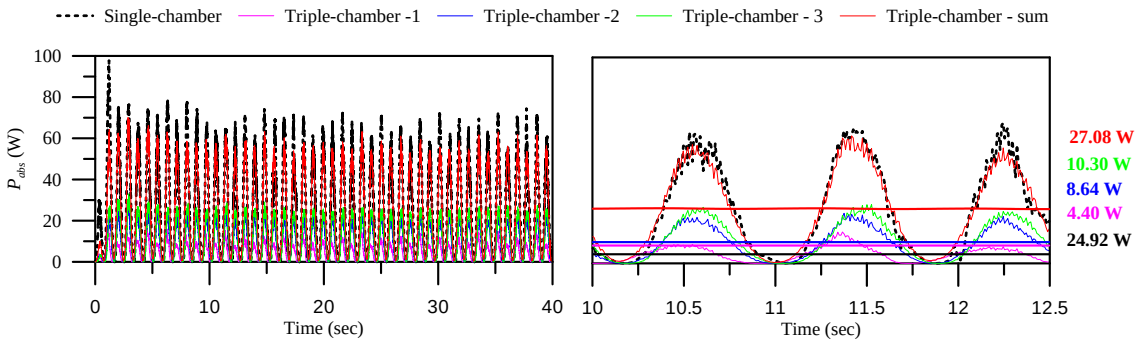

Fig. 7 Power output comparison between single- and triple-chamber OWC configurations for kh=1.26

Table 4 Variation in power output with lip-wall depth across different chamber configurations

No. of chambers	Constant depth variation	P_{abs} (W)
Single	d_1	24.92
	d_2	24.98
	d_3	19.5
Double	d_1	27.37
	d_2	25.48
	d_3	16.92
Triple	d_1	23.34
	d_2	22.21
	d_3	13.35

The study was extended to examine the effects of increasing the lip-wall depth from d_1 = 0.15, to d_2 and d_3. The resulting power outputs have been summarized in Table 4. When comparing the percentage ratios of power output between d_1, d_2, and d_3 across the different chamber

configurations, it was found that increasing the lip-wall depth from d_1 to d_2 had a minimal impact on change of power output, with ratios of 100%, 93%, and 95% for the single-, double-, and triple-chambers, respectively. However, further increasing the depth from d_1 to d_3 resulted in significantly decreased power outputs, with ratios of 78%, 62%, and 57% for the single-, double-, and triple-chambers, respectively. These findings indicate that the depth d_1 produces the highest power output, suggesting that increasing the lip-wall depth to higher levels does not yield substantial benefits in power generation.

6.3 Training and testing of ML models

In this section, a comprehensive investigation into the performance evaluation of the OWC for single-, double-, and triple-chambers shall be analyzed using each ML model, as detailed in Section 4 and given in Tables 1-3. A comparative study aims to assess the applicability of each ML model and its ability to recognize the underlying patterns in the input data generated through CFD, considering different combinations of hyperparameters. The performance of each ML model has been evaluated based on the magnitude of the error, estimated using Mean Squared Error (MSE) and R^2 score. To evaluate model performance, the dataset was divided using an 80:20 train-validation split, where 80% of the data was used to train the model, enabling it to learn underlying patterns, while the remaining 20% was reserved for validation to assess how well the model generalizes to unseen data. Different combinations of hyperparameters for the various machine learning models have been considered. These include: Selection of polynomial regression by applying models of degree 1, 2, 3, and 4, where the degree of the polynomial—serving as a measure of model complexity—was systematically varied to evaluate its effect on OWC performance. In decision tree, the maximum depth of the tree was tested to examine how it affects the model's performance. For the random forest model, two key hyperparameters were explored: number of estimators (gives the number of trees in the forest) and maximum depth (gives the maximum depth for each individual tree). SVR tested with C: values of 1,10, and 100 and for kernel coefficient of RBF kernel (gamma) range of values, including 0.01, 0.1 and 1, was considered; e : different epsilon values such as 0.01, 0.1, and 1 were examined to determine the model's sensitivity to errors. In regards with the XGBoost model three key hyperparameters were explored: the learning rate (LR), with values including 0.01 and 0.2; the maximum depth of the trees; and the number of estimators. Finally, MLP regression model LR with 0.001, 0.005, 0.01, and 0.05 were tested. Hidden layer sizes ($H1$, $H2$): the number of neurons in the first and second hidden layers was varied, with the combinations of 16, 32, 64, and 128 being considered. For each combination of these hyperparameters, the models were run, and the corresponding error values were calculated.

It is evident from the results that, for the single-chamber data, the MLP regression model outperforms the other models in terms of predictive accuracy see Table 5. The MLP model achieved an MSE of 1.58 and a high R^2 score of 0.98, indicating that it is able to explain 98% of the variance in the data. This suggests that the MLP model is highly effective at capturing the underlying patterns and relationships in the single-chamber data, leading to accurate predictions. In contrast, for the double-chamber data, the SVR model emerged as the most effective model. With an MSE of 1.37 and an R^2 score of 0.98, the SVR model demonstrated small errors in predictions and a robust fit to the data. The relatively low MSE and the high R^2 score suggest that SVR was particularly well-suited for this type of data, efficiently handling the complexity of the relationships between features while keeping the prediction error minimal. Furthermore, the study

Table 5 Error matrix for different ML models

No. of Chambers	Metric	Polynomial Regression	Decision Tree	Random Forest	SVR	XG Boost	MLP Regression
Single	MSE	1.66	12.67	10.19	2.39	4.27	1.58
	R^2	0.97	0.84	0.87	0.97	0.88	0.98
Double	MSE	3.35	10.86	5.33	1.37	1.75	9.24
	R^2	0.95	0.86	0.93	0.98	0.97	0.88
Triple	MSE	9.77	2.89	2.44	1.35	1.37	2.71
	R^2	0.88	0.96	0.97	0.98	0.98	0.96

Table 6 Performance error matrix of different ML models on combined data set of single-, double-, and triple-chamber OWC

ML Model	MSE	R^2
Polynomial Regression	4.81	0.94
Decision Tree	8.84	0.904
Random Forest	4.51	0.95
SVR	2.97	0.96
XG Boost	1.68	0.98
MLP Regression	2.18	0.97

extended to the triple-chamber data, where it was found that the SVR performed well, with errors very close to those of the double-chamber model, compared to the other models. Despite the limited input data provided to the selected models, SVR consistently yielded better performance, resulting in minimal error values. This highlights the importance of identifying the optimal set of hyperparameters for each model, as this directly influences the model's performance (See Table 5). By carefully tuning hyperparameters, the error can be minimized, and the model can be made more efficient in making accurate predictions.

The entire dataset combining the single-, double-, and triple-chambers of OWC into one single set of input data by comprising various features and input variables, has been utilized to train the ML models. A total of five distinct ML models were trained and tested, with the primary focus on evaluating their performance. Table 6 presents a comprehensive comparison of the performance of each ML model, including detailed evaluation metrics from the error matrix. The results clearly demonstrate that XGBoost consistently outperforms the other models, achieving the lowest MSE and the highest coefficient of determination R^2 scores. This suggests that XGBoost is better suited for the given predictive data compared to the other ML models in terms of accuracy and precision. The identified set of hyperparameters with the XGBoost model for various hyperparameter combinations were explored. Specifically, the LR was tested at four different values: 0.01, 0.05, 0.1, and 0.2. Additionally, the number of estimators was varied across three values: 50, 100, and 200. The maximum tree depth (depth) was adjusted to values of 3, 5, and 7. These hyperparameters were systematically combined to form a comprehensive set of experiments. Notably, the combination of a LR of 0.2, 200 estimators, and a depth of 3 yielded the lowest MSE

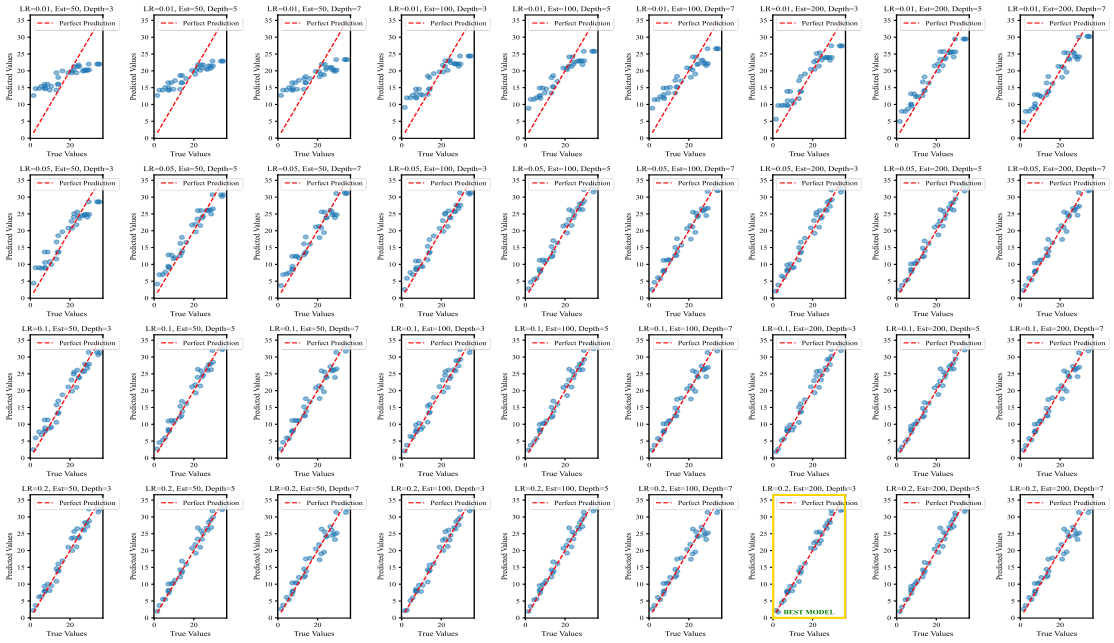

Fig. 8 Hyperparameter combinations and their true and predicted values using XGBoost model

and the highest R^2 score compared to all other combinations, with values of 1.68 and 0.98, respectively (see Figs. 8 and 9). This combination of hyperparameters proved to be the most effective in reducing prediction error and improving model accuracy. This quantification allows for a clear comparison of how different hyperparameter configurations impact model performance, providing insight into the sensitivity of the XGBoost model to these parameters.

6.4 Design optimization

To perform the design optimization based on the available range of each input variable for different OWC configurations, a total of 1,000 distinct design configurations were generated with range of combinations as $\{ (d_1, d_2, d_3, \theta, T, \phi) \mid d_1 \in [0, 0.15], d_2 \in [0, 0.30], d_3 \in [0, 0.45], \theta \in [0°, 30°], T \in [2.0, 5.5], \phi \in [1.0, 9.0] \}$. These configurations were generated using the latin hypercube sampling (LHS) method, which allows for efficient and systematic sampling across the entire range of each input parameter. By employing LHS, the full spectrum of minimum and maximum values associated with each input variable is effectively captured, ensuring a comprehensive and diverse exploration of the design space. This method of sampling is also particularly advantageous because it maintains a high level of statistical coverage while avoiding redundancy and clustering, which often occur in purely random sampling approaches. The generated LHS dataset was then analyzed to examine the distribution of each input variable in terms of its probability density (PD). Fig. 10 illustrates the PD plots for all input features based on the LHS-generated data. From the figure, it is evident that the distributions maintain an approximately uniform spread across the defined ranges for each parameter. This uniformity confirms that the sampling process adequately spans the design space, allowing us to investigate

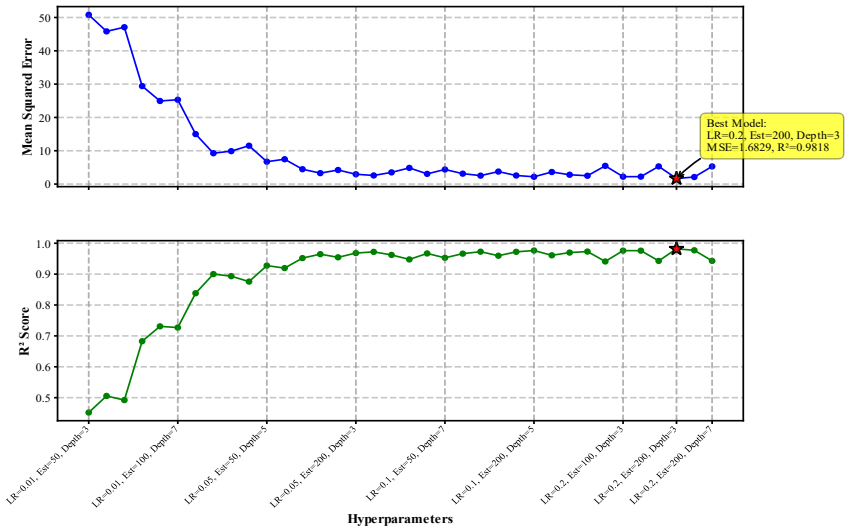

Fig. 9 MSE and R^2 score variation with different hyperparameter combinations for XGBoost model

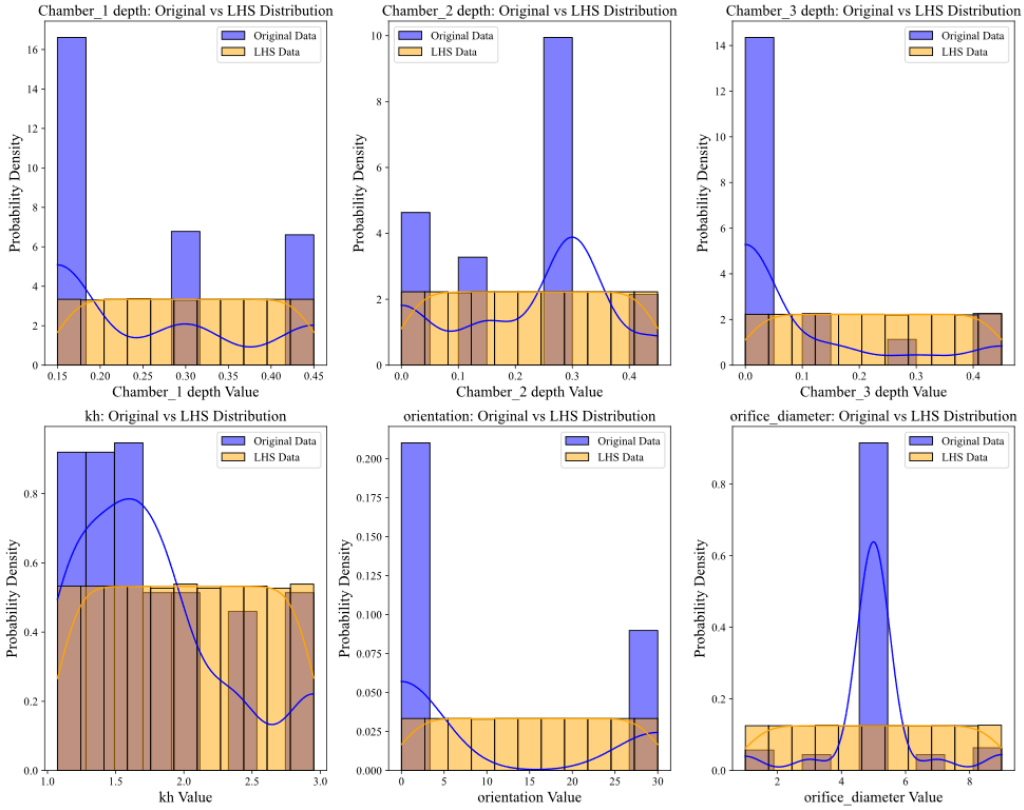

Fig. 10 LHS and original data probability distribution for various OWC parameters

Table 7 Top ten OWC configurations

OWC design combination	d_1 (m)	d_2 (m)	d_3 (m)	kh	Orientation (°)	Orifice diameter (mm)	Predicted power (W)
1	0.19	0.40	0.0	1.10	29	3.1699	36.40
2	0.19	0.40	0.0	1.12	7	4.9466	36.40
3	0.42	0.36	0.0	1.14	26	3.5391	36.30
4	0.44	0.22	0.10	1.12	16	4.4512	36.27
5	0.23	0.04	0.12	1.12	10	4.5383	35.85
6	0.19	0.21	0.0	1.20	14	4.0899	35.12
7	0.28	0.15	0.0	1.24	8	4.9945	35.12
8	0.20	0.13	0.0	1.23	6	3.8026	34.50
9	0.24	0.40	0.0	1.12	19	6.0348	34.25
10	0.30	0.33	0.14	1.13	11	5.5767	34.25

the impact of various combinations of input variables on the overall performance of the OWC system.

The following Table 7 presents the optimal combination of design parameters for the OWC system, as determined through data-driven optimization using LHS. These configurations have been ranked based on their effectiveness in maximizing power extraction.

Among the various design setups analysed, the configuration yielding the highest extracted power-measured at 36.40 W-corresponds to a dual-chamber OWC. This optimal configuration consists of chamber depths d_1 = 0.19 m and d_2 = 0.40 m, an orientation angle of 7° and 29°, and orifice diameters of 3.17 mm and 4.95 mm, respectively. These specific parameter values have demonstrated higher energy capture under the given wave conditions.

To address if any possibility of the ML model extrapolating beyond the valid range of its training data—particularly given that the predicted power output is approximately 33% higher than the numerical simulation results, as shown in Tables 4 and 7—a thorough evaluation was conducted to determine whether predictions fall outside the supported input space. Three well-established extrapolation diagnostic techniques were employed:

- Bounds check: Input feature values associated with high-power predictions were verified to lie within the range observed during training. Bounds check technique confirms that the model does not extrapolate beyond the absolute limits of the training dataset for any input parameter.
- Mahalanobis distance: This statistical measure assesses how far a new input instance is from the multivariate mean of the training data, accounting for correlations among features. Based on a standard threshold, approximately 17.5% of the top power predictions were flagged as potential outliers, indicating that some inputs are relatively distant from the core distribution of the training set.
- Isolation forest: This anomaly detection technique identifies statistically rare or isolated data points through random partitioning. Only 6.2% of the high-power predictions were flagged as anomalous. Notably, the optimal design configuration was not flagged by this method, suggesting it lies within a well-represented region of the input space.

Overall, these diagnostics indicate that although the model generally operates within the bounds of the training data, a subset of high-power predictions originates from sparsely sampled regions. Thus, even though the optimal prediction appears to be supported by the training data, results in less densely populated areas of the input space should be interpreted with caution (see Fig. 10). In overall, while machine learning models offer strong predictive capabilities, they should be applied carefully and not assumed to generalize beyond the data on which they were trained.

Furthermore, the majority of the top-performing configurations consist predominantly of dual-chamber systems, with only a few instances of triple-chamber designs appearing among the top- ranking power outputs. This trend strongly suggests that, within the parameter space explored in this study, dual-chamber OWCs generally outperform other configurations in terms of energy extraction efficiency. These findings provide valuable insights into the influence of chamber geometry and orientation on power performance. However, to validate and extend the practical applicability of these results, further investigations are recommended. Specifically, future studies should focus on testing the optimal configurations under irregular wave conditions and at a prototype or full scale. Such work is already in progress to assess the feasibility and robustness of the current design recommendations.

7. Conclusions

This study demonstrates the effectiveness of a CFD-ML hybrid framework for the design and performance optimization of multi-chamber OWC wave energy converters. The numerical model was validated against the experimental results of Morris-Thomas *et al.* (2007), showing good agreement in power output and hydrodynamic behavior across a range of *kh* values. A series of 176 CFD simulations were performed, covering various geometrical and wave parameters. These high-fidelity results were then used to train ML models to predict power output and guide the optimization process. Some of the important conclusions from this study are:

- The CFD results showed a strong correlation with experimental benchmarks, especially near the resonance condition ($kh \approx 1.26$), confirming the model's accuracy.
- Transitioning from a single-chamber to a double-chamber resulted in a 12% increase in power output (from 24.92 W to 27.37 W). The triple-chamber setup offered only marginal improvement (~11%), indicating diminishing returns.
- Among all trained models, XGBoost achieved the highest predictive accuracy, with an R^2 score of 0.98 and a MSE of 1.68, making it the most reliable for design predictions across all chamber configurations.
- Using LHS over 1,000 design combinations, the best-performing configurations were dual-chamber OWCs, with predicted peak power outputs of up to 36.4 W. The top two configurations had: d_1= 0.19 m; d_2 = 0.40 m; lip-wall orientations: 7° and 29° and orifice diameters: 3.17 mm and 4.95 mm.
- Finally, a dual-chamber configuration offers the best trade-off between geometric complexity and energy performance.

Acknowledgments

The third author gratefully acknowledges the financial support provided by NFIG

(SB23241953OENFIG009070) for this work. We also extend our sincere thanks to Prof. Bae for initiating this collaborative research with IITM.

References

Ananthu, P., Shanas, P.R., Komath, S., Sivakrishnan, K.K. and Kumar, V.S. (2025), "Wave climate of Kerala Coast: An 83-Year ERA-5 study of trends and seasonality", *Earth Syst. Environ.*, 1-22. https://doi.org/10.1007/s41748-024-00561-3.

Chowdhury, P., Behera, M.R. and Reeve, D.E. (2019), "Wave climate projections along the Indian coast", *Int. J. Climatol.*, **39**(11), 4531-4542. https://doi.org/10.1002/joc.6096.

Cui, Y., Liu, Z., Zhang, X. and Xu, C. (2019), "Review of CFD studies on axial-flow self-rectifying turbines for OWC wave energy conversion", *Ocean Eng.*, **175**, 80-102. https://doi.org/10.1016/j.oceaneng.2019.01.040.

Elhanafi, A. and Kim, C.J. (2018), "Experimental and numerical investigation on wave height and power take–off damping effects on the hydrodynamic performance of an offshore–stationary OWC wave energy converter", *Renew. Energ.*, **125**, 518-528. https://doi.org/10.1016/j.renene.2018.02.131.

Faedo, N. and Ringwood, J.V. (2024), "A control framework for ocean wave energy conversion systems: The potential of moments", *Annu. Rev. Control Robot. Autonom. Syst.*, **7.** https://doi.org/10.1146/annurev-control-070523-115155.

Falcão, A.F. and Henriques, J.C. (2016), "Oscillating-water-column wave energy converters and air turbines: A review", *Renew. Energ.*, **85**, 1391-1424. https://doi.org/10.1016/j.renene.2015.07.086.

Filianoti, P.G., Gurnari, L., Torresi, M. and Camporeale, S.M. (2018), "CFD analysis of the energy conversion process in a fixed oscillating water column (OWC) device with a Wells turbine", *Energ. Procedia*, **148**, 1026-1033. https://doi.org/10.1016/j.egypro.2018.08.058.

Gayathri, R., Chang, J.Y., Tsai, C.C. and Hsu, T.W. (2024), "Wave energy conversion through oscillating water columns: A review", *J. Mar. Sci. Eng.*, **12**(2), 342. https://doi.org/10.3390/jmse12020342.

George, A., Cho, I.H. and Kim, M.H. (2021), "Optimal design of a U-shaped oscillating water column device using an artificial neural network model", *Processes*, **9**(8), 1338. https://doi.org/10.3390/pr9081338

Gurnari, L., Filianoti, P.G. and Camporeale, S.M. (2022), "Fluid dynamics inside a U-shaped oscillating water column (OWC): 1D vs. 2D CFD model", *Renew. Energ.*, **193**, 687-705. https://doi.org/10.1016/j.renene.2022.05.025.

Han, M.M. and Wang, C.M. (2021), "Coupled analytical-numerical approach for determining hydrodynamic responses of breakwater with multiple OWCs", *Mar. Struct.*, **80**, 103097. https://doi.org/10.1016/j.marstruc.2021.103097.

Heath, T.V. (2012), "A review of oscillating water columns", *Philos. T. Roy. Soc. A: Math. Phys. Eng. Sci.*, **370**(1959), 235-245. https://doi.org/10.1098/rsta.2011.0164.

Karimirad, M. (2014), *Offshore energy structures: for wind power, wave energy and hybrid marine platforms*. Springer. https://doi.org/10.1007/978-3-319-12175-8.

Kassayeva, A., Balekova, A. and Yerzhanov, K. (2024), "Converting the energy of sea waves into electrical energy", *Environ. Progress Sust. Energ.*, **43**(3), e14342. https://doi.org/10.1002/ep.14342.

Kim, J.S., Nam, B.W., Park, S., Kim, K.H., Shin, S.H. and Hong, K. (2022), Numerical investigation on hydrodynamic energy conversion performance of breakwater-integrated oscillating water column-wave energy converters", *Ocean Eng.*, **253**, 111287. https://doi.org/10.1016/j.oceaneng.2022.111287.

Liu, Z., Xu, C., Kim, K. and Li, M. (2022), "Experimental study on the overall performance of a model OWC system under the free-spinning mode in irregular waves", *Energy*, **250**, 123779. https://doi.org/10.1016/j.energy.2022.123779.

López, I., Carballo, R., Taveira-Pinto, F. and Iglesias, G. (2020), "Sensitivity of OWC performance to air compressibility", *Renew. Energ.*, **145**,1334-1347. https://doi.org/10.1016/j.renene.2019.06.076.

Mahnamfar, F. and Altunkaynak, A. (2017), "Comparison of numerical and experimental analyses for optimizing the geometry of OWC systems", *Ocean Eng.*, **130**, 10-24. https://doi.org/10.1016/j.oceaneng.2016.11.054

Malara, G. and Arena, F. (2013), "Analytical modelling of an U-oscillating water column and performance in random waves", *Renew. Energy*, **60**, 116-126. https://doi.org/10.1016/j.renene.2013.04.016.

Morris-Thomas, M.T., Irvin, R.J. and Thiagarajan, K.P. (2007), "An investigation into the hydrodynamic efficiency of an oscillating water column", *J. Offshore Mech. Arct.*, **129**(4), 273-278. https://doi.org/10.1115/1.2426992

Moñino, A., Medina-López, E., Clavero, M. and Benslimane, S. (2017), "Numerical simulation of a simple OWC problem for turbine performance", *Int. J. Mar. Energ.*, **20**, 17-32. https://doi.org/10.1016/j.ijome.2017.11.004

Natarajan, S.K., George, A. and Cho, I.H. (2024), "Optimal design of an inclined barrier for performance improvement of an oscillating water column device with an artificial neural network model", *Ocean Eng.*, **310**, 118679. https://doi.org/10.1016/j.oceaneng.2024.118679.

Ning, D.Z., Shi, J., Teng, B. and Zhao, H.T. (2014), "Numerical simulation of a land-based oscillating water column wave energy conversion device", *J. Harbin Engi. Univ.*, **35**(7), 789-794. http://dx.doi.org/10.3969/j.issn.1006-7043.201306002.

Rao, R., Raj, H., Vipin, V. and Koley, S. (2024), July. "Power generation prediction of OWC device using deep neural network model", *Proceedings of the 2024 3rd International Conference on Electrical, Electronics, Information and Communication Technologies (ICEEICT)*, 1-8. IEEE. https://doi.org/10.1109/ICEEICT61591.2024.10718532.

Rosati, M., Henriques, J.C.C. and Ringwood, J.V. (2022), "Oscillating-water-column wave energy converters: A critical review of numerical modelling and control", *Energ. Convers. Manage. X*, **16**, 100322. https://doi.org/10.1016/j.ecmx.2022.100322.

Shalby, M., Elhanafi, A., Walker, P. and Dorrell, D.G. (2019), "CFD modelling of a small–scale fixed multi–chamber OWC device", *Appl. Ocean Res.*, **88**, 37-47. https://doi.org/10.1016/j.apor.2019.04.003.

Singh, U., Abdussamie, N. and Hore, J. (2020), "Hydrodynamic performance of a floating offshore OWC wave energy converter: An experimental study", *Renew. Sust. Energ. Rev.*, **117**, 109501. https://doi.org/10.1016/j.rser.2019.109501.

Singh, U., Rizwan, M., Malik, H. and García Márquez, F.P. (2022), "Wind energy scenario, success and initiatives towards renewable energy in India—A review", *Energies*, **15**(6), p.2291. https://doi.org/10.3390/en15062291.

Vipin, V., Trivedi, K. and Koley, S. (2023), "Optimization of parameters of the OWC wave energy converter device using MLP and XGBoost models", *Results in Phys.*, **55**, 107163. https://doi.org/10.1016/j.rinp.2023.107163.

Yang, B., Duan, J., Chen, Y., Wu, S., Li, M., Cao, P. and Jiang, L. (2024), "A critical survey of power take-off systems based wave energy converters: Summaries, advances, and perspectives", *Ocean Eng.*, **298**, 117149. https://doi.org/10.1016/j.oceaneng.2024.117149.

Zabihi, M., Mazaheri, S. and Namin, M.M. (2019), "Experimental hydrodynamic investigation of a fixed offshore oscillating water column device", *Appl. Ocean Res.*, **85**, 20-33. https://doi.org/10.1016/j.apor.2019.01.036.

Zhao, M. and Ning, D. (2024), "A review of numerical methods for studying hydrodynamic performance of oscillating water column (OWC) devices", *Renew. Energ.*, 121177. https://doi.org/10.1016/j.renene.2024.121177.

Zhou, Y., Ning, D., Liang, D. and Cai, S. (2021), "Nonlinear hydrodynamic analysis of an offshore oscillating water column wave energy converter", *Renew. Sust. Energ. Rev.*, **145**, 111086. https://doi.org/10.1016/j.rser.2021.111086.